Author/s:
Ji, Y;Zhao, X;Pan, Y;Su, Z;Lin, J;Akinoglu, EM;Xu, Y;Zhang, H;Zhao, P;Dong, Y;Wei, X;Liu, F;Mulvaney, P

Title:
CuSCN Modified Back Contacts for High Performance CZTSSe solar cells

Date:
2023-01-05

Citation:
Ji, Y., Zhao, X., Pan, Y., Su, Z., Lin, J., Akinoglu, E. M., Xu, Y., Zhang, H., Zhao, P., Dong, Y., Wei, X., Liu, F. & Mulvaney, P. (2023). CuSCN Modified Back Contacts for High Performance CZTSSe solar cells. Advanced Functional Materials, 33 (11), https://doi.org/10.1002/adfm.202211421.

Persistent Link:
https://hdl.handle.net/11343/325172

ADVANCED FUNCTIONAL MATERIALS
www.afm-journal.de

CuSCN Modified Back Contacts for High Performance CZTSSe Solar Cells

Yixiong Ji, Xiangyun Zhao, Yining Pan, Zhenghua Su, Jinhong Lin, Eser Metin Akinoglu, Yang Xu, Heyou Zhang, Pengjun Zhao, Yue Dong, Xingzhan Wei, Fangyang Liu, and Paul Mulvaney**

Optimization of the back contact interface is crucial for improving the performance of Cu_2ZnSnS_4 (CZTS) thin film solar cells. In this paper, self-depleted CuSCN is deployed as an intermediate layer at the Mo/CZTS interface to improve the quality of the back contact. This CuSCN layer, obtained via aqueous solution processing, reduces the thickness of $Mo(S,Se)_2$ and eliminates multi-layer crystallization of the absorber by suppressing the undesirable reaction between Mo and Se during the selenization process. By regulating the selenium infiltration into the CZTS precursor films during the selenization process, highly crystalline, single-layer $Cu_2ZnSn(S,Se)_4$ (CZTSSe) absorber layers are realized. The single-layer CZTSSe absorber exhibits reduced carrier recombination, enhanced carrier density and increased work function. The improved back contact and absorber layer enables 11.1% power-conversion-efficiency to be achieved.

1. Introduction

There is an ongoing search for new photovoltaic (PV) materials for thin-film solar cells, which require lower energy and materials input than silicon-based PV systems, which dominate current production. $Cu_2ZnSn(S,Se)_4$ (CZTSSe) is one of the most promising absorber materials for thin film photovoltaic applications because it comprises earth abundant elements and, unlike other candidates, it is both air-stable and moisture-resistant.[1,2] Currently 13% power conversion efficiencies have been reported for lab-scale CZTSSe PV cells, based on solution processing in DMSO.[3] However, this value still lags behind competitors such as perovskite and $Cu(In,Ga)SSe_2$. One of the keys to erasing this gap is through improvements to the back contact between Mo and CZTSSe.[4–8]

Better design of the back contact interface is essential for improving the performance of CZTSSe solar cells.[7,8] The decomposition of CZTSSe induced by the Mo back contact during heat treatment drives the formation of highly undesirable secondary phases such as Cu_2Se, ZnSe, SnSe, and $Mo(S,Se)_2$ as well as voids at this back interface.[9] These voids and secondary phases are not only detrimental for charge transport at the back contact, they also generate multilayer structures within the absorber materials.[10] In turn, defects within the grain boundaries and interfaces between these layers generate recombination centers for charge carriers. Furthermore, the thick $Mo(S,Se)_2$ layers increase the series resistance and drag down the fill factor (FF) and consequently the overall solar energy conversion efficiency. To solve these problems, thermally stable interlayers based on materials such as TiN, TiB_2, carbon, ZnO or Al_2O_3, have been deposited between CZTSSe and Mo to prevent selenium from diffusing into the Mo film.[11–15] However such CZTSSe solar cells still exhibit compromised performance

Y. Ji, E. M. Akinoglu, Y. Xu, H. Zhang, P. Mulvaney
ARC Centre of Excellence in Exciton Science
School of Chemistry
University of Melbourne
Victoria 3010, Australia
E-mail: mulvaney@unimelb.edu.au
Y. Ji, X. Zhao, Y. Pan, F. Liu
School of Metallurgy and Environment
Central South University
Changsha 410083, China
E-mail: liufangyang@csu.edu.cn

The ORCID identification number(s) for the author(s) of this article can be found under https://doi.org/10.1002/adfm.202211421.

DOI: 10.1002/adfm.202211421

Z. Su, J. Lin
Shenzhen Key Laboratory of Advanced Thin Films and Applications
College of Physics and Optoelectronic Engineering
Shenzhen University
Shenzhen 518060, China
E. M. Akinoglu
International Academy of Optoelectronics at Zhaoqing
South China Normal University
Zhaoqing, Guangdong 526238, China
P. Zhao
Xinjiang Technical Institute of Physics and Chemistry
Chinese Academy of Sciences
Urumqi 830011, China
Y. Dong
Leibniz-Institut für Polymerforschung Dresden e.V. Institute of Physical Chemistry and Polymer Physics
01069 Dresden, Germany
X. Wei
Chongqing Institute of Green and Intelligent Technology
Chinese Academy of Sciences
Chongqing 400714, China

because of their lower electrical conductivity. The addition of these interlayers also introduces the need to precisely control the layer thickness during vacuum processing, which increases the complexity of fabrication. Conversely, it has been demonstrated that Ag, Bi, and Na_2S interlayers do not introduce extraneous materials into the device because Ag, Bi, and Na can migrate into the CZTS lattice and, in these cases, the depleted interlayer can lead to improved PV performance, as well as a greater tolerance toward variations in layer thickness.[16–18]

Here we introduce a solution-based, self-depleted CuSCN thin film as an intermediate layer to inhibit decomposition reactions at the Mo/CZTSSe contact. The goal is to reduce the formation of $Mo(S,Se)_2$ and crystallographic defects while still enabling high temperatures to be used to drive selenization and grain growth of CZTSSe. The unfavorable multi-layer structure of the CZTSSe absorber is eliminated as well. Indeed, we demonstrate that CuSCN dramatically improves not only the back contact characteristics but also the quality of the CZTSSe absorber layer in solution processed CZTSSe solar cells.

2. Results and Discussion

2.1. Single-Layer Structure of CZTSSe Layer

The CuSCN intermediate layer was deposited on Mo-coated soda lime glass substrate by spin-coating the 10 mg mL^{-1} precursors dissolved in either diethyl sulfide (DES) or ammonia-water mixtures.[19,20] Then the samples were baked at 120 °C for 15 min to remove the solvents. After that, a CZTSSe absorber layer with a thickness of ≈1.5 µm was deposited on both Mo glass as a control sample and onto Mo glass coated with the CuSCN film. A 2-methoxyethanol-based precursor solution was employed for the CZTS and following deposition, the films were annealed at 550 °C in a selenium atmosphere. Further details about the preparation of the CZTS precursor solution and the deposition conditions can be found in previous work.[21] Energy Dispersive Spectrometer (EDS) measurements were used to determine the elemental composition, from which we found mole ratios of: Cu/(Zn+Sn) ≈0.75 and Zn/Sn ≈1.2 (Figures S4

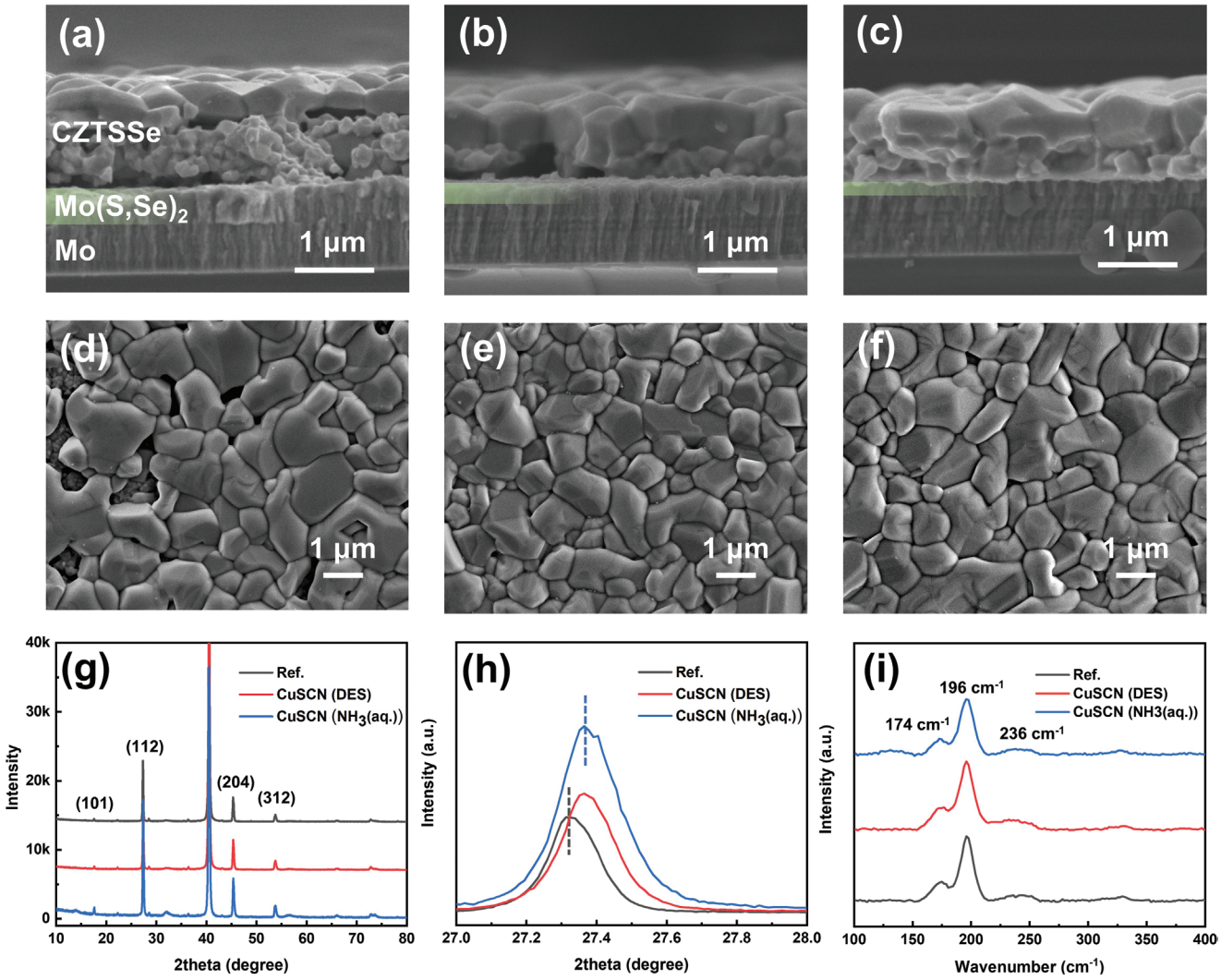

Figure 1. Cross-sectional SEM images of a): CZTSSe films on Mo, b): CuSCN (DES)/Mo films and c): CuSCN (NH_3(aq.))/Mo. Top-view SEM images of CZTSSe films on Mo d), CuSCN (DES)/Mo e) and CuSCN (NH_3(aq.))/Mo f). g) XRD patterns of selenized CZTSSe films: reference (black), with CuSCN (DES) (red) and CuSCN (NH_3(aq.)) (blue). h) (112) peaks of CZTSSe in the above samples. i) Raman spectra.

and S5, Supporting Information). Surface and cross-sectional SEM images of the selenized CZTSSe films with and without CuSCN as an intermediate layer are displayed in **Figure 1**. Both diethyl sulfide (DES) and ammonia-water mixtures are popular solvents for dissolving CuSCN powder.[20,22] The spin-coated CuSCN film is fully depleted during the selenization process and cannot be discerned in the SEM images. The formation of a 400 nm thick $Mo(S,Se)_2$ interfacial layer for the device without a CuSCN layer is evident between the Mo layer and CZTSSe absorbers. This $Mo(S,Se)_2$ layer thickness is strongly reduced to ≈150 nm when a 40 nm CuSCN film is inserted as an intermediate layer. We also observe that there is a more uniform and pin-hole-free surface morphology in the presence of CuSCN. Remarkably, the fine-grain layer is eliminated and voids are also inhibited significantly, which should reduce charge carrier recombination and improve device performance.

To investigate the influence of the CuSCN intermediate layer on the crystallinity of the CZTSSe absorber, XRD and Raman measurements were taken, and the results are shown in Figure 1(g–i). Both the XRD patterns and the Raman spectra demonstrate that the crystallographic structure of the samples is kesterite CZTSSe (JCPDS #01-070-8930), and there is no evidence for secondary phases such as $CuSe_x$, $SnSe_x$ or Cu_2SnSe_3, which indicates that the thin CuSCN intermediate layer does not lead to the formation of unfavorable secondary phases in the CZTSSe absorber.[23] Comparison of the (112) XRD diffraction peaks for each sample, which are presented in Figure 1(h), reveals that the CZTSSe absorber with a CuSCN intermediate layer prepared from an ammonia-water mixture exhibits the best crystallinity. This is consistent with the cross-sectional morphology shown in Figure 1(c).

2.2. Mechanism of Improved Grain Growth Through Local Chemical Atmosphere Engineering by CuSCN at the Back Contact

A diagram illustrating CZTSSe crystallization and growth processes is presented in **Figure 2** to help explain how CuSCN influences the grain growth. Figure 2(a) shows the normal process used to prepare CZTSSe, which usually results in a thick, fine-grained layer underneath the absorber due to insufficient Se penetration. This occurs because gas exchange pathways are prematurely closed off by the formation of larger grains. To prevent the formation of the undesirable fine-grained layer, a high-pressure selenization process can be used, as shown in Figure 2(b). Driven by a high vapor pressure of 0.02 MPa, Se penetration is significantly improved and it now reaches the Mo/CZTS interface. However, excessive Se leads to the crystallization of Cu_xSe at the back contact[24] and this layer of Cu_xSe at the bottom surface then grows upward. The process in the presence of a CuSCN modified back contact under high Se pressure is shown in Figure 2(c). Due to the mismatch in thermal expansion coefficients of CuSCN (negative expansion coefficient) and CZTS (positive expansion coefficient), there is a significant shear stress created at the interface between CZTSSe and CuSCN, which eliminates the undesired grain growth at the back contact during the initial stages of the selenization process. The calculated thermal stress distributions are shown in Figure S3 (Supporting Information). A strong contractile force is generated in the region near the CuSCN/CZTSSe interface at the bottom of the absorber (shown in Figure S3b, Supporting Information), which reduces the infiltration of selenium even at high Se pressures until the CuSCN is completely decomposed.

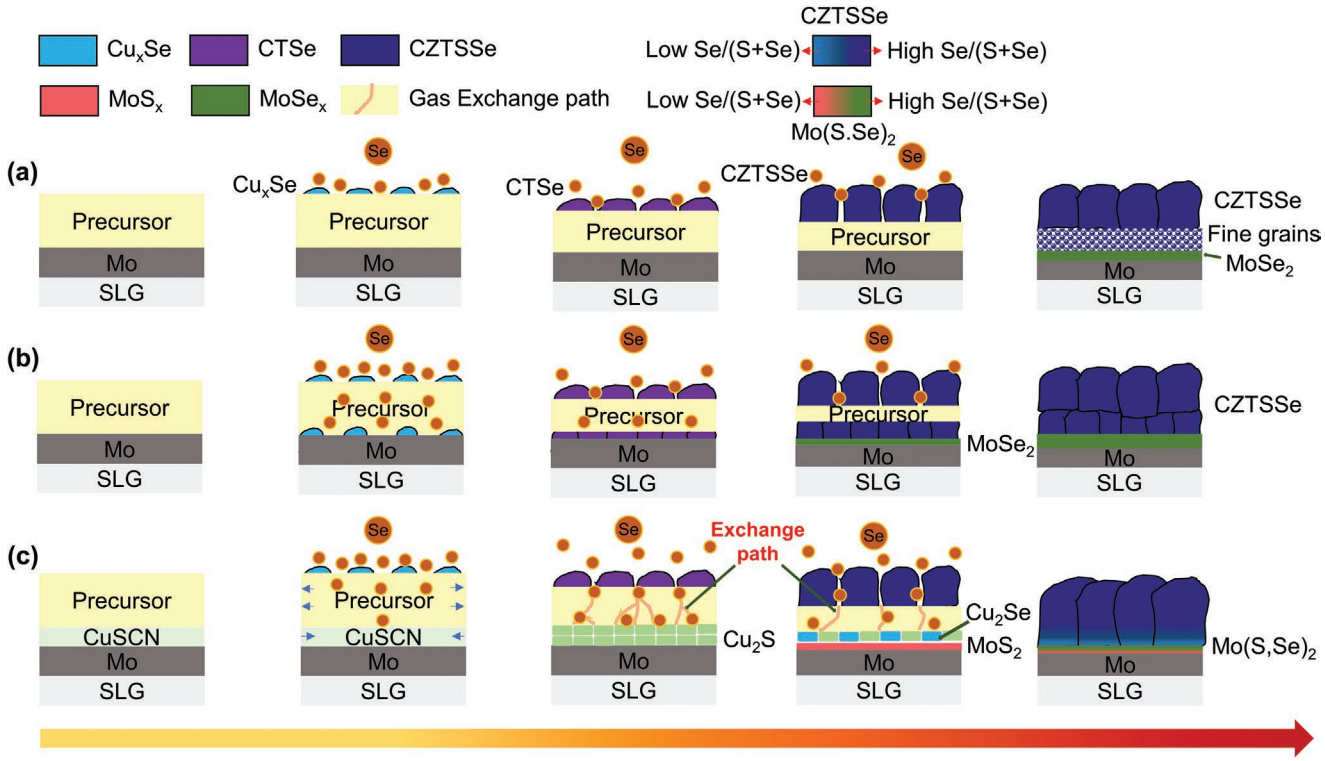

Figure 2. Diagram illustrating CZTSSe crystallization and growth processes a) without CuSCN under atmospheric pressure, b) without CuSCN under high pressure (0.02 MPa), and c) with CuSCN under high pressure. The small arrows in c) show the directions of thermal expansion.

Table 1. The photovoltaic and diode parameters of the best solar cells fabricated without and with CuSCN (DES). The values of E_g are obtained from the EQE data. The diode parameters are extracted using Site's methods[24,25].

Device	Voc [V]	Jsc [mA cm^{-2}]	FF [%]	PCE [%]	A	J_0 [mA cm^{-2}]	Rs [ohm cm^{-2}]	Rsh [ohm cm^{-2}]	Eg/q-V_{OC} [V]	E_{PL} [eV]
Ref.	0.4529	33.5452	58.4326	8.8770	2.82	3.17×10^{-2}	1.13	227.4	0.647	1.01
CuSCN (DES)	0.4802	35.9619	64.3091	11.0900	1.76	1.93×10^{-3}	0.54	611.6	0.630	1.02

2.3. The Influence of Depleted CuSCN on the Photovoltaic Performance

The photovoltaic performance parameters of CZTSSe devices with and without a CuSCN intermediate layer, including open circuit voltage (V_{OC}), short-circuit current density (J_{SC}), fill factor (FF), and power conversion efficiency (PCE), are shown in Figure S10 (Supporting Information). Devices with CuSCN do not show much difference in overall PCE when prepared using different solvents. The use of ammonia-water as the solvent for CuSCN leads to a marginal improvement in V_{OC}. However, the use of a volatile ammonia-water mixture can lead to some sacrifice in FF. Conversely, the most uniform FF is achieved for devices prepared with CuSCN (DES) as the solvent but in this case, there is some compromise in V_{OC}. In general, the CuSCN layer leads to significant improvements in J_{SC}, V_{OC}, and FF and the average PCE increases from ≈8.4% to ≈10.7% with an optimal cell achieving a PCE of 11.1% (CuSCN (DES)). Based on the SEM, XRD, and Raman results, the enhanced performance is attributed to the elimination of voids, thinner $Mo(S,Se)_2$ at the back contact, and improved bulk crystallinity. For a more detailed analysis of the PV performance, the parameters for two champion cells with CuSCN (DES) and without (reference) are summarized in **Table 1**. *J–V* curves and EQE data are displayed in **Figure 3**. Specifically, V_{OC} increases from 453 mV for the reference device to 480 mV for the one with CuSCN (DES), while J_{SC} increases from 33.5 to 35.9 mA cm^{-2}. The larger J_{SC} of the device with CuSCN (DES) is ascribed to the thinner, high-resistance $Mo(S,Se)_2$ film (see Figure 1(b)). In addition, an obvious decrease in series resistance and an increase in shunt resistance also contribute to the higher FF of the device with CuSCN (DES) (Table 1). A better carrier collection efficiency is evident from the comparison of the EQE spectra (Figure 3(d)). The improvement in response right across the long wavelength regime from 550 to 1000 nm is attributed to both the significantly increased minority carrier lifetimes and diffusion lengths, as well as to better carrier collection and the reduction in carrier recombination inside the absorber layer in the CuSCN (DES) device.[25] Due to the formation of low Se/(S+Se) ratio CZTSSe in the CuSCN sample, the bandgap calculated from the EQE spectrum in Figure 3(e) is slightly higher than that of the reference sample. In Figure 3(f) we have used the Urbach tail model to characterize the variation in the band tail states. The values derived from the inverse of the slope for the linear portion below the bandgaps are almost the same (≈21.5 meV) for the above two devices, indicating similar

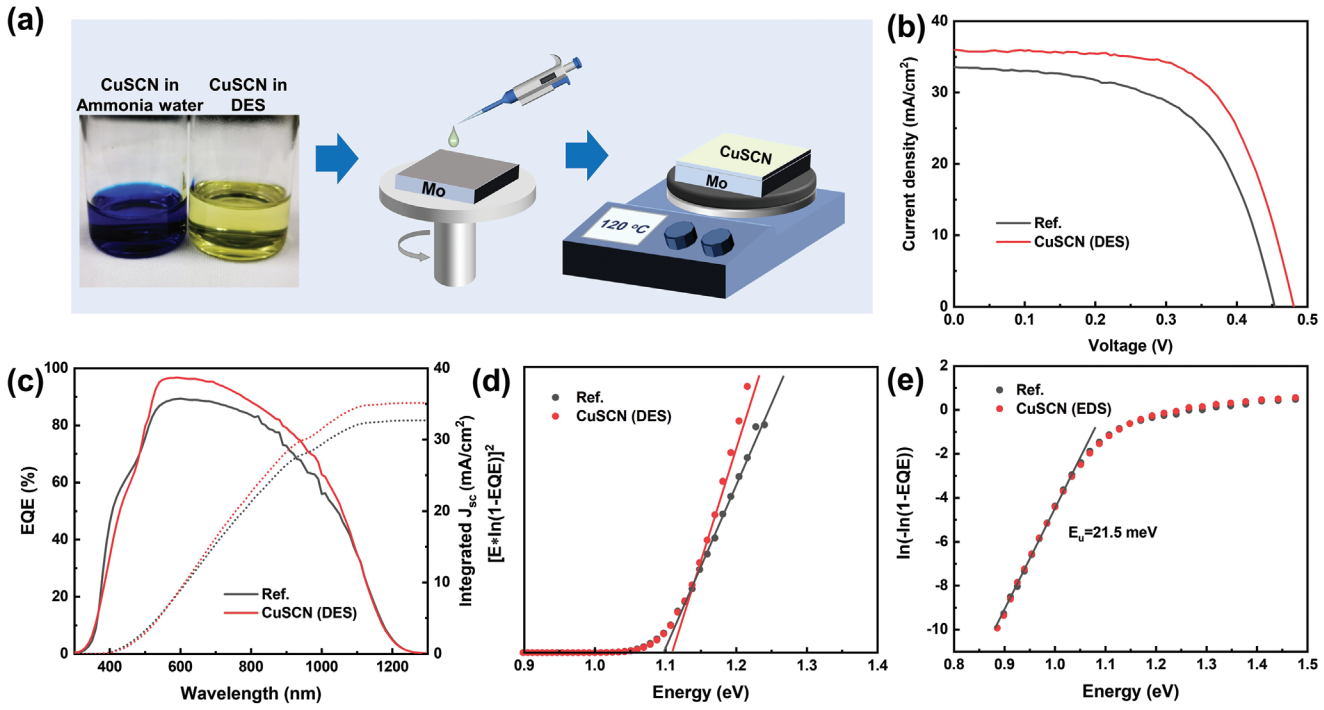

Figure 3. a) Schematic structure of spin-coated CuSCN on Mo glass. b) *J–V* curves in the presence and absence of CuSCN. c) EQE spectra and integrated J_{SC} of CZTSSe solar cells in the presence and absence of CuSCN. d) The bandgaps were determined by plotting $[E*\ln(1\text{-EQE})]^2$ versus Energy (eV). e) Urbach energy of CZTSSe solar cells calculated from the EQE spectra in the presence and absence of CuSCN.

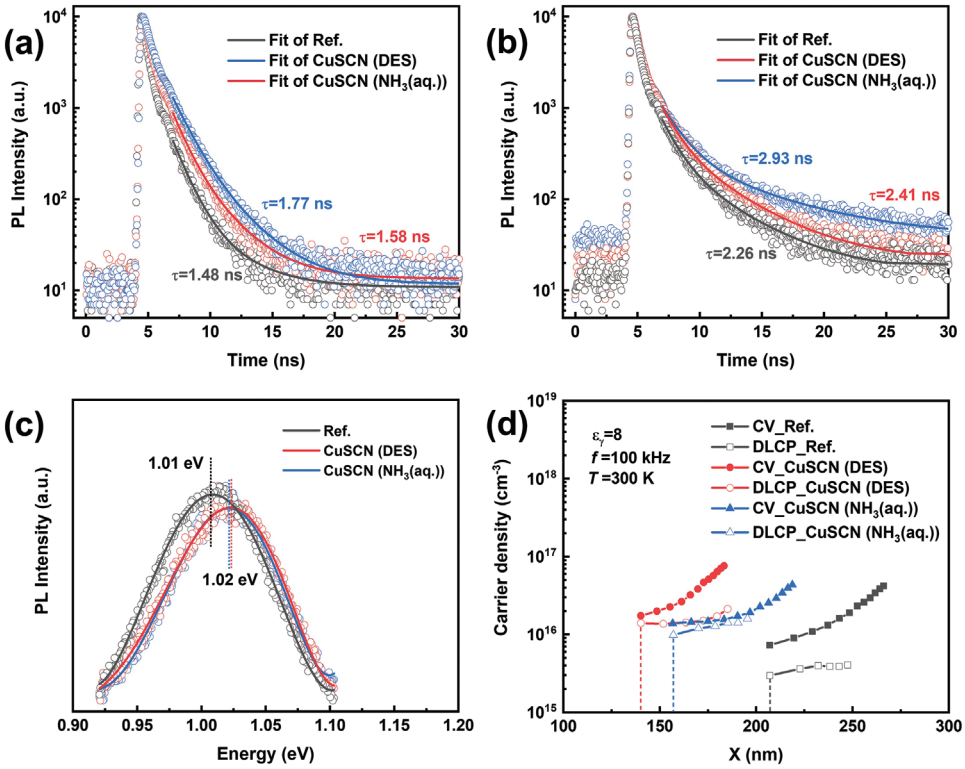

Figure 4. a), b) TRPL decay spectra for the reference, CuSCN (DES) and CuSCN (NH_3(aq.)) samples excited by lasers at 532 and 800 nm, respectively. c) The steady-state PL spectra following laser excitation at 532 nm. d) CV-DLCP Curves. The dashed line indicates the depletion width at 0 V bias.

tail states are present in both devices. Therefore, the higher V_{oc} value is likely to be a consequence of the suppressed recombination; there is also a decrease in the interface defect density within the solar cell, which will be discussed later.

Room temperature photoluminescence spectroscopy (PL) and time resolved photo-luminescence spectroscopy (TRPL) measurements were carried out on the champion CZTSSe device to investigate the mechanisms underpinning the recombination process and the minority carrier lifetime. The recombination processes reduce the effective bandgap of the absorber, leading to significant V_{OC} loss.[25,28] **Figures 4**(a,b) show the TRPL decay data of the devices with and without self-depleted CuSCN, measured using laser excitation at 532 and 800 nm respectively. The excitation at 532 nm generates carriers mostly at the p–n junction interface and in the very top region of the CZTSSe absorber, whereas the 800 nm laser generates charge carriers more uniformly distributed throughout the bulk.[29] By fitting the TRPL spectra collected using 532 nm excitation to a bi-exponential function, the effective lifetimes (τ_{avg}) were determined to be 1.58 and 1.77 ns for the CuSCN (DES) and CuSCN (NH_3(aq.)) devices respectively, which are both slightly higher than the lifetime found for the reference sample (1.48 ns). The extracted lifetimes for the (CuSCN (DES)) and (CuSCN (NH_3(aq.))) devices were 2.41 and 2.93 ns respectively when excited at 800 nm and these are again longer than the 2.26 ns lifetime found for the reference sample. This improved carrier lifetime demonstrates that the cells with depleted CuSCN suffer less carrier recombination, both in the heterojunction region and deep in the CZTSSe bulk. This is a direct consequence of the formation of a highly crystalline, single-layer absorber. As shown in Figure 4(c), the normalized PL emission peaks of the samples with and without depleted CuSCN are quite broad and located at 1.01 and 1.02 eV, respectively, both of which are lower than the bandgap, E_g, determined from the EQE data (Figure 3(d)). In addition, the difference in energy between the optical absorption edge and the PL peak (≈0.09 eV) for the above two samples suggests that the devices still suffer from detrimental, nonradiative recombination processes.[26]

To further study the carrier density and collection properties of the CZTSSe absorbers, the capacity-voltage (C-V) profile and drive-level capacity profile (DLCP) are presented in Figure 4(d). The charge density, width of the depletion region (W_d) and defect densities in the depletion region derived from C-V and DLCP data are listed in **Table 2**. These values explain

Table 2. Summary of the results derived from C–V and DLCP measurements.

Device	N_{CV} [cm^{-3}]	N_{DL} [cm^{-3}]	V_{bi} [V]	Depletion width [nm]	Interface state response [relative values]
Device_Ref.	7.29×10^{15}	2.97×10^{15}	0.54	207.0	4.3×10^{15}
Device_CuSCN (DES)	1.73×10^{16}	1.39×10^{16}	0.62	140.2	3.4×10^{15}
Device_CuSCN (NH3(aq.))	1.38×10^{16}	9.83×10^{15}	0.60	156.7	4.0×10^{15}

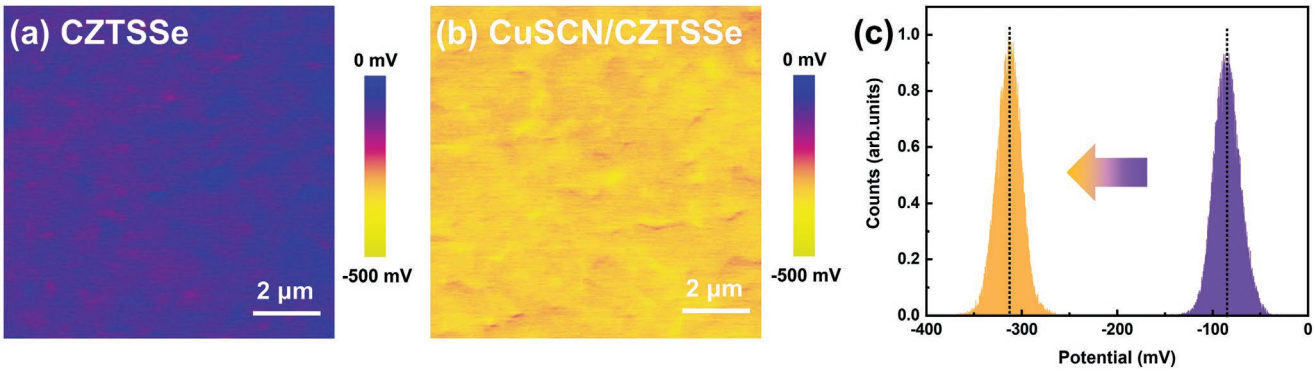

Figure 5. KPFM generated surface potential maps of a) a CZTSSe film after annealing and b) a CuSCN/CZTSSe film after annealing; c) the mean contact potential differences (CPD) of each film calculated by averaging across the values at each pixel in each film.

the trends in charge separation and collection efficiencies of the PV devices.[28] The CuSCN (DES) and CuSCN (NH_3(aq.)) samples with high charge densities generally show narrower depletion widths, consistent with previous reports.[30] Specifically, we find higher carrier densities (1.73×10^{16} and 1.38×10^{16} cm^{-3} for the CuSCN(DES) and CuSCN (NH_3(aq.)) devices respectively, compared to 7.29×10^{15} cm^{-3} for the reference sample) and correspondingly shorter depletion regions (140 and 157 nm versus 207 nm). Indeed these carrier densities are close to those reported for other high performance CZTSSe devices fabricated by researchers at IBM (1.0×10^{16} cm^{-3}) and DGIST (1.8×10^{16} cm^{-3}).[31,32] The difference between the carrier density derived from C-V (N_{CV}) and DLCP (N_{DL}) at zero bias is attributed to acceptor-like interface trap states (N_{IT}) at the CZTS/CdS heterojunction.[28,32] Assuming that these interface trap states are uniformly distributed within the depletion region, the density of interface trap states can be roughly estimated using: $N_{IT} = N_{CV} - N_{DL}$.[33,34] The calculated trap state densities for the different samples are shown in Table 2. The interface trap state density does not change with doping density. This also implies that the Cu content is not the only factor affecting the depletion region in our case. The improved crystallinity of the absorber leads to a reduction in the density of interface trap states and a better contact to the *n*-type CdS layer.

KPFM images have been employed to map the contact potential difference (CPD) distribution across the bare CZTSSe samples and these range from −135 to −40 mV, whereas for the CuSCN/CZTSSe films the CPD values range from −365 to −265 mV. The mean CPD value for CuSCN/CZTSSe sample lies at a more negative potential than the mean CPD value of the reference film (from −87 to −310 mV shown in **Figure 5**(c)). A higher CPD implies a higher Fermi level and lower work function.[5] Obviously, the CZTSSe absorber with depleted CuSCN exhibits a lower surface Fermi level, indicating it has a higher carrier concentration (*p*-type material), in agreement with the above CV and DLCP results. The lower Fermi level also suggests that there will be a larger quasi-Fermi level offset when forming a *p-n* junction, leading to larger band bending, higher V_{OC}, and better cell performance.

3. Conclusion

In summary, we have demonstrated an efficient back contact modification method for CZTSSe solar cells. By inserting a self-depleted CuSCN thin layer at the CZTS/Mo interface, enhanced crystallinity of the CZTSSe absorber layer is achieved. This leads to a 20% increase in PCE. The device analysis reveals that the formation of $Mo(S,Se)_2$ and secondary phases at the back contact are effectively suppressed by the CuSCN intermediate layer during high temperature selenization. Further investigation reveals that unfavorable multi-layer crystallization behavior is obviated and a more crystalline, single-layer CZTSSe absorber layer is created in the presence of CuSCN. As a consequence, the photoelectrical transport properties both within the bulk absorber and at the contact between CZTSSe and CdS are improved significantly, thereby also improving the performance of CZTSSe solar cells substantially.

Supporting Information

Supporting Information is available from the Wiley Online Library or from the author.

Acknowledgements

Y.J. and X.Z. contributed equally to this work. This work was funded by the National Key Research and Development Program of China (2018YFE0203400), the ARC Centre of Excellence in Exciton Science through ARC Grant CE170100026, and by the Guangdong Innovative and Entrepreneurial Team Program (No. 2016ZT06C517). The authors acknowledge support from DISR through the Australia-China Science Research Fund (Grant ACSRIII000001). Y.J. would like to thank Dr. Wei Yao from the University of Electronic Science and Technology of China for Raman measurements.

Open access publishing facilitated by The University of Melbourne, as part of the Wiley - The University of Melbourne agreement via the Council of Australian University Librarians.

Conflict of Interest

The authors declare no conflict of interest.

Data Availability Statement

The data that support the findings of this study are openly available in Minerva Elemants at https://minerva-elements.unimelb.edu.au, reference number 9999.

Keywords

CuSCN, CZTS, back contacts, PV, solar cells

Received: October 2, 2022
Revised: December 6, 2022
Published online:

[1] K. I. Nakazawa, *Jpn. J. Appl. Phys.* **1988**, *27*, 2094.
[2] S. K. Wallace, D. B. Mitzi, A. Walsh, *ACS Energy Lett.* **2017**, *2*, 776.
[3] M. A. Green, E. D. Dunlop, J. Hohl-Ebinger, M. Yoshita, N. Kopidakis, X. Hao, *Progress in Photovoltaics: Research and Applications* **2022**, *30*, 3.
[4] K. F. Tai, O. Gunawan, M. Kuwahara, S. Chen, S. G. Mhaisalkar, C. H. A. Huan, D. B. Mitzi, *Adv. Energy Mater.* **2016**, *6*, 1501609.
[5] J. Wang, J. Zhou, X. Xu, F. Meng, C. Xiang, L. Lou, K. Yin, B. Duan, H. Wu, J. Shi, *Adv. Mater.* **2022**, *34*, 2202858.
[6] D. Wang, W. Zhao, Y. Zhang, S. F. Liu, *J. Energy Chem.* **2018**, *27*, 1040.
[7] V. Karade, A. Lokhande, P. Babar, M. G. Gang, M. Suryawanshi, P. Patil, J. H. Kim, *Sol. Energy Mater. Sol. Cells* **2019**, *200*, 109911.
[8] P. D. Antunez, D. M. Bishop, Y. S. Lee, T. Gokmen, O. Gunawan, T. S. Gershon, T. K. Todorov, S. Singh, R. Haight, *Adv. Energy Mater.* **2017**, *7*, 1602585.
[9] J. J. Scragg, J. T. Watjen, M. Edoff, T. Ericson, T. Kubart, C. Platzer-Bjorkman, *J. Am. Chem. Soc.* **2012**, *134*, 19330.
[10] Q. Yu, J. Shi, L. Guo, B. Duan, Y. Luo, H. Wu, D. Li, Q. Meng, *Nano Energy* **2020**, *76*, 105042.
[11] W. Li, J. Chen, H. Cui, F. Liu, X. Hao, *Mater. Lett.* **2014**, *130*, 87.
[12] F. Liu, J. Huang, K. Sun, C. Yan, Y. Shen, J. Park, A. Pu, F. Zhou, X. Liu, J. A. Stride, *NPG Asia Mater.* **2017**, *9*, e401.
[13] F. Liu, K. Sun, W. Li, C. Yan, H. Cui, L. Jiang, X. Hao, M. A. Green, *Appl. Phys. Lett.* **2014**, *104*, 051105.
[14] F. Zhou, F. Zeng, X. Liu, F. Liu, N. Song, C. Yan, A. Pu, J. Park, K. Sun, X. Hao, *ACS Appl. Mater. Interfaces* **2015**, *7*, 22868.
[15] B. Shin, Y. Zhu, N. A. Bojarczuk, S. Jay Chey, S. Guha, *Appl. Phys. Lett.* **2012**, *101*, 053903.
[16] H. Cui, X. Liu, F. Liu, X. Hao, N. Song, C. Yan, *Appl. Phys. Lett.* **2014**, *104*, 041115.
[17] Z. Tong, K. Zhang, K. Sun, C. Yan, F. Liu, L. Jiang, Y. Lai, X. Hao, J. Li, *Sol. Energy Mater. Sol. Cells* **2016**, *144*, 537.
[18] Y. Gu, H. Shen, C. Ye, X. Dai, Q. Cui, J. Li, F. Hao, X. Hao, H. Lin, *Adv. Funct. Mater.* **2018**, *28*, 1703369.
[19] Y. Ji, J. Yang, W. Luo, L. Tang, X. Bai, C. Leng, C. Ma, X. Wei, J. Wang, J. Shen, *ACS Appl. Mater. Interfaces* **2018**, *10*, 9571.
[20] N. Wijeyasinghe, A. Regoutz, F. Eisner, T. Du, L. Tsetseris, Y. H. Lin, H. Faber, P. Pattanasattayavong, J. Li, F. Yan, *Adv. Funct. Mater.* **2017**, *27*, 1701818.
[21] X. Zhao, Y. Pan, C. Zuo, F. Zhang, Z. Huang, L. Jiang, Y. Lai, L. Ding, F. Liu, *Sci. Bull.* **2021**, *66*, 880.
[22] W. Luo, C. Zeng, X. Du, C. Leng, W. Yao, H. Shi, X. Wei, C. Du, S. Lu, *J. Mater. Chem. C* **2018**, *6*, 4895.
[23] P. M. Salomé, P. A. Fernandes, J. P. Leitao, M. G. Sousa, J. P. Teixeira, A. F. da Cunha, *J. Mater. Sci.* **2014**, *49*, 7425.
[24] J. Tuttle, M. Contreras, M. Bode, D. Niles, D. Albin, R. Matson, A. Gabor, A. Tennant, A. Duda, R. Noufi, *J. Appl. Phys.* **1995**, *77*, 153.
[25] J. Li, Wang, M. Luo, J. Tang, C. Chen, W. Liu, F. Liu, Y. Sun, J. Han, Y. Zhang, *Sol. Energy Mater. Sol. Cells* **2016**, *149*, 242.
[26] J. Li, Y. Huang, J. Huang, G. Liang, Y. Zhang, G. Rey, F. Guo, Z. Su, H. Zhu, L. Cai, *Adv. Mater.* **2020**, *32*, 2005268.
[27] A. Collord, H. Hillhouse, *Chem. Mater.* **2016**, *28*, 2067.
[28] J. Li, J. Huang, Y. Huang, H. Tampo, T. Sakurai, C. Chen, K. Sun, C. Yan, X. Cui, Y. Mai, *Sol. RRL* **2021**, *5*, 2100418.
[29] C. Yan, J. Huang, K. Sun, S. Johnston, Y. Zhang, H. Sun, A. Pu, M. He, F. Liu, K. Eder, *Nat. Energy* **2018**, *3*, 764.
[30] Z. Su, J. M. R. Tan, X. Li, X. Zeng, S. K. Batabyal, L. H. Wong, *Adv. Energy Mater.* **2015**, *5*, 1500682.
[31] D.-H. Son, S.-H. Kim, S.-Y. Kim, Y.-I. Kim, J.-H. Sim, S.-N. Park, D.-H. Jeon, D.-K. Hwang, S.-J. Sung, J.-K. Kang, *J. Mater. Chem. A* **2019**, *7*, 25279.
[32] W. Wang, M. T. Winkler, O. Gunawan, T. Gokmen, T. K. Todorov, Y. Zhu, D. B. Mitzi, *Adv. Energy Mater.* **2014**, *4*, 1301465.
[33] G.-X. Liang, Z.-X. Yu, Z.-G. Xie, Y. He, J.-H. Lin, S. Chen, Z.-H. Zheng, J.-T. Luo, P. Fan, Z.-H. Su, *Sol. RRL* **2021**, *5*, 2100574.
[34] H. S. Duan, W. Yang, B. Bob, C. J. Hsu, B. Lei, Y. Yang, *Adv. Funct. Mater.* **2013**, *23*, 1466.